Modulated porous wick evaporator for loop heat pipes: Experiment

CrossMark

Jinliang Xu [a,*], Xianbing Ji [b], Wolong Yang [b], Ziwei Zhao [b]

[a] State Key Laboratory of Alternate Electrical Power System with Renewable Energy Sources, North China Electric Power University, Beijing 102206, China
[b] The Beijing Key Laboratory of Multiphase Flow and Heat Transfer, North China Electric Power University, Beijing 102206, China

ARTICLE INFO

ABSTRACT

The available studies indicate the significantly enhanced pool boiling heat transfer by the modulated porous wick sintered on the heater wall. This paper sinters the modulated porous wick as the primary wick on the evaporator wall for loop heat pipes (LHPs). Three types of evaporators were fabricated to integrate with other LHP components: MWE (microchannel/wick evaporator), MME (modulated monoporous wick evaporator) and MBE (modulated biporous wick evaporator). Experiments were performed with water as the working fluid at various tilt angles. The major findings are (1) MBE LHP significantly shortens start-up time and stabilizes all temperatures during the steady operation; (2) MBE LHP decreased the evaporator wall temperatures by 20~50 °C at moderate or high heat loads compared with MWE LHP at similar conditions; (3) MBE LHP achieved the evaporator wall temperature of 63 °C at the heat load of 200 W for the anti-gravity operation, under which the heat flux attained 40 W/cm², which is 1.7~6.7 times of those reported in references; (4) MBE behaves the nucleate boiling heat transfer at small head loads, and film evaporation heat transfer at moderate or large heat loads; (5) A properly designed MBE LHP achieved better performance when the evaporator is above the condenser; (6) Effect of liquid charge ratios was studied with the best liquid charge ratio of 51.3%. The best geometric parameters for porous stacks and vapor channels, as well as the best particle size were obtained.

The MBE multiscale behavior majorly accounts for the performance improvement: small pores (~µm scale) creating great capillary force for liquid suction, large pores (~10 µm scale) between clusters increasing surface area for liquid film evaporation, and vapor channels (~mm scale) for vapor venting. Besides, small contact thermal resistance and reduced heat flow path in the evaporator also improve the LHP performance.

© 2014 Elsevier Ltd. All rights reserved.

1. Introduction

Evaporator is an important component for a loop heat pipe (LHP) [1]. The porous material within an evaporator has the following functions: thermal conduction through wicks, vapor generation and release within porous pores, and liquid supply due to the capillary force with small pores. These functions are affected by parameters such as particle size, porosity, permeability and wick layer thickness, etc. The exact relationship among these effects is not exactly known yet.

Boiling/evaporation heat transfer on a porous coating surface involves vapor generation, release and liquid supply. The liquid supply is related to capillary pressure of $\Delta p = 4\sigma \cos \theta_c / d_e$. A small pore size is needed to create sufficient capillary pressure for liquid circulation. Now we consider the vapor venting into the vapor channel of a LHP. Meléndez and Reyes [2] gave vapor mass flow rate from the porous media as

$$m = \frac{\pi}{128} \left(\frac{\rho_v \sigma}{\mu_v} \right) \left(\frac{\varepsilon d_e^3}{\delta} \right) \tag{1}$$

It is seen from Eq. (1) that a larger pore size achieves a larger vapor mass flow rate.

The above analysis indicates that the liquid supply and vapor release require different pore sizes. A small pore size is helpful for the liquid supply towards the phase change surface but hinders the vapor escape into the vapor channel.

There are two evaporator types for LHPs in the literature: cylindrical evaporator [3] and flat plate evaporator [4]. This paper focuses on the flat plate evaporator. Fig. 1 shows the internal evaporator structure for LHP (conventional design). Parallel microchannels are machined on the evaporator substrate. There is a wick layer above microchannels, functioning as the liquid supply and evaporation within the porous layer.

Evaporator thermal resistance consists of the thermal resistance of evaporator wall, the thermal resistance of microchannels, the contact thermal resistance between microchannel tips and wick layer, and the thermal resistance within porous layer. Because phase

* Corresponding author. Tel.: +86 10 61772268.
E-mail address: xjl@ncepu.edu.cn (J. Xu).

Nomenclature

A	heater area on the wall, m^2
D_e	evaporator diameter, m
D_{ei}	wick layer diameter, m
d_e	effective pore diameter, m
d_p	particle diameter, m
h	porous stack height, m
L_l	liquid line length, m
m	mass flow rate, kg/s
p	vapor channel width, m
Q	heat load, W
Δp	pressure drop, Pa
q	heat flux, W/m^2
R	thermal resistance, K/W
r	radial coordinate, m
T	temperature, K
w	porous stack width, m
z	extended tube length, m

Greek symbols

α	heat transfer efficient, W/m^2 K
δ	thickness of porous covers, m
ε	porosity of wick
ϕ	liquid charge ratio

μ	viscosity, kg/m s
θ	tilt angles of LHP, °
θ_c	contact angle , °
ρ	density, kg/m^3
σ	surface tension force, N/m

Subscripts

C	center wall of evaporator
Cin	condenser inlet
$Cout$	condenser outlet
CP	compensation chamber
$CPin$	compensation chamber inlet
$C1{\sim}C4$	location on condenser tube line
$Eout$	vapor outlet port
eva	evaporator
l	liquid
LHP	loop heat pipe
max	maximum
min	minimum
V	vapor tube line
v	vapor
$1{\sim}8$	location on evaporator wall

change heat transfer majorly happens within the porous layer above microchannels, heat transfer through microchannels is majorly due to the heat conduction. At high heat fluxes, formerly a monoporous wick was intolerant of boiling and easily occupied by vapor to form a vapor blanket, leading to raise the thermal resistance. The evaporator temperature is increased due to very low thermal conductivity of a vapor blanket layer [5]. Another issue for LHP evaporator is the heat leakage. The generated vapor has the possibility to contact with liquid in the compensation chamber. This will increase the heat leakage, which decrease the temperature difference between evaporator and compensation chamber and prevent fluid circulation to worsen the LHP performance. In the extreme case, the liquid circulation is stopped and the LHP does not work.

Recent progress on evaporator improvement puts biporous wick above microchannels. Biporous wick has two distinct characteristic pore sizes. Large pores exist between powder clusters, increasing the surface area for liquid film evaporation and decreasing the flow resistance for the vapor venting to the downward microchannels. Small pores exist between particles, creating capillary force to supply liquid. Semenic and Catton [6] examined

the pool boiling heat transfer on biporous wick surface. The best thick biporous wick reaches a critical heat flux of 990 W/cm^2 (147 °C superheat) with water as the working fluid. The top wick layer supplies liquid to the evaporating menisci above the vapor blanket, vapor jets form between large pores of the wick and vent vapor out of the wick. Yeh et al. [7] analyzed heat transfer of a biporous wick LHP. At the heat sink temperature of 10 °C and the evaporator temperature of 85 °C, the evaporative heat transfer coefficient of the biporous wick, which reached a maximum value of 64 kW/m^2 K, was approximately six times higher than that of the monoporous wick. Lin et al. [5] proposed a mathematical model of evaporative heat transfer in a LHP. The evaporator wick was assumed to have three regions: a vapor blanket, a two-phase region, and a saturated liquid region. The biporous wick shows distinct heat transfer characteristic and higher performance compared with monoporous wick. Recently, Liu et al. [8] experimentally investigated a LHP, in which biporous wick and stainless steel mesh screen were adopted as the primary and secondary wicks. The LHP sustains 80 W heat load with the evaporator wall temperature below 85 °C, and the LHP thermal resistance lies
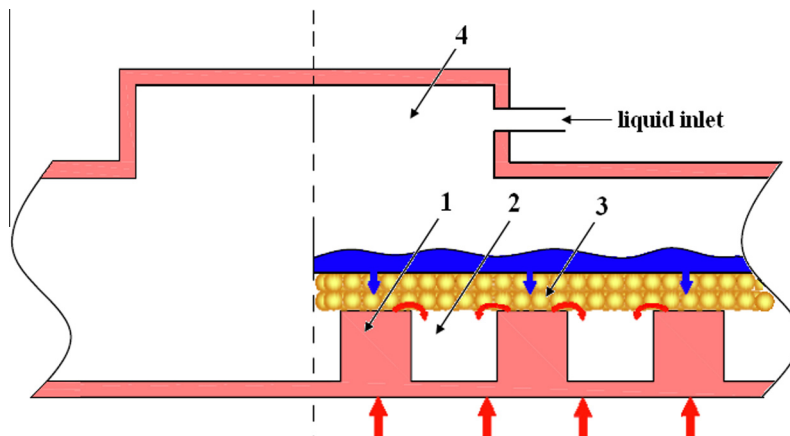
Fig. 1. The conventional MWE (microchannel/wick evaporator, 1: microchannel fin, 2: microchannel, 3: porous wick, 4: compensation chamber).

between 0.46 °C/W and 2.28 °C/W. Tang et al. [9] used the graded pore size wick to fabricate a LHP, having the anti-gravity function.

This paper integrates the modulated porous wick within a LHP evaporator. The modulated porous wick refers to porous stacks sintered on the evaporator wall and vapor channels between porous stacks (see Fig. 2). Microchannels are not used. The modulated porous wick separates flow paths of vapor and liquid. Liquid is supplied within the porous stacks by the capillary force and evaporation happens at the solid–liquid–vapor interface. The modulated porous wick satisfies the requirement of large valley size for vapor venting and small pore size for liquid suction. The modulated porous wick was recently studied for pool boiling heat transfer enhancement. Min et al. [10] showed that the critical heat fluxes on the modulated porous coating surface can be 2.0 to 3.3 times of those on plain surface. Ji et al. [11] showed the 3.7 times of critical heat fluxes on the modulated porous coating surface compared with the plain surface, maximally. But the modulated porous wick for LHP evaporators is not reported previously. This paper found that if fine particles are sintered on the evaporator wall, the porous stacks also behave the biporous wick characteristic: large pores appear between particle clusters and small pores exist between particles. The biporous wick behavior significantly increases the surface area for liquid film evaporation and large pores can vent vapor to the vapor channel (see Fig. 2).

Because heat evaporates liquid into vapor within porous stacks adjacent to the evaporator wall, the secondary monoporous wick and third wick layer not only function as the liquid supplier, but also function as the hydraulic and thermal barriers (see Fig. 2). The third wick layer had ultra-low thermal conductivity. The objective of this approach is to:

- fabricate three types of LHPs: MWE (microchannel/wick evaporator) LHP (conventional design), MME (modulated/monoporous wick evaporator) LHP, and MBE (modulated/biporous wick evaporator) LHP;

- measure thermal performance of the three types of LHPs with water as the working fluid;
- explore the effect of liquid charge ratio, tilt angle, particle size, etc. on the LHP performance;
- reach the best modulated porous wick evaporator for LHPs.

2. Experimental setup and measurement

2.1. The loop heat pipe

Fig. 3a shows the LHP and Table 1 shows the major parameters. Copper is the main material to fabricate the LHP, consisting of an evaporator integrated with a compensation chamber, a vapor line, a fin-tube condenser and a liquid line. A set of evaporators were prepared with different internal structures (see Section 2.2 for details). All the evaporator had the same outer diameter of 80.0 mm and the thickness of 10.0 mm (not including the compensation chamber height).

The LHP contains a commercial fin-tube condenser, having a planar size of 130 mm by 130 mm with a thickness of 25.0 mm. There are totally 53 pieces of aluminum fins, each with a 0.2 mm thickness. The gap between neighboring fins is 2.0 mm. The forced convective air dissipates heat to the environment. The power driving the fan is 5.0 W. The environment temperature is controlled to be within 22~24 °C. Both vapor line and liquid line tubes had an outer diameter of 8.0 mm and an inner diameter of 6.0 mm.

A snake-shaped thin film heater provides the Joule heat to the evaporator (including two identical parts, see Fig. 3b). The film heater was symmetrically attached on the bottom evaporator surface. The heater had an effective heating area of 5.0 cm². The silver silica gel with high thermal conductivity was filled between the film heater and the evaporator surface. This heating method decreases the system thermal inertia and heat loss to the environment. The film heater was driven by an adjustable DC voltage

(a) planar view of the primary modulated biporous layer

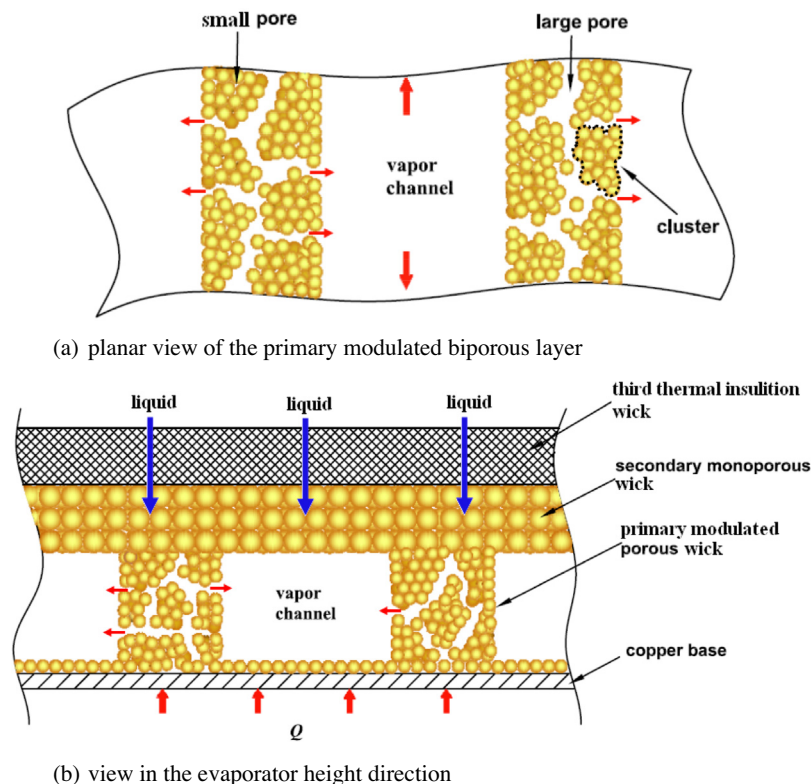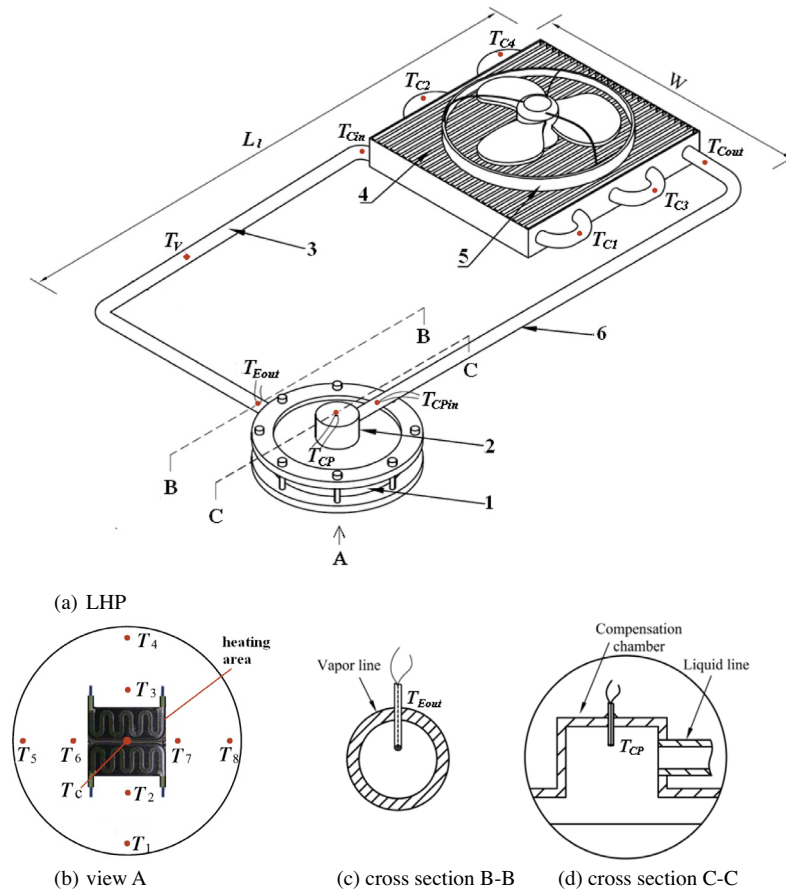(b) view in the evaporator height direction

Fig. 2. The modulated porous wick evaporator in planar and height direction views.

Fig. 3. The loop heat pipe for experiment (1: evaporator, 2: compensation chamber, 3: vapor line, 4: condenser fin, 5: fan, 6: liquid line).

Table 1
The loop heat pipe parameters.

LHP material	Copper
Porous material	Copper powders and absorbent wool
Planar LHP size	300.0 mm length by 300.0 mm width
Evaporator diameter and thickness	D_e = 80.0 mm with 10.0 mm thickness
Evaporator wall thickness	1.0 mm
Internal evaporator diameter	72.0 mm
Vapor line length	550.0 mm
Vapor tube outer/inner diameters	8.0 mm/6.0 mm
Condenser size	130.0 mm (length) × 130.0 mm (width) × 25.0 mm (thickness)
Heating area	2.5 cm × 2.0 cm = 5.0 cm^2
Liquid line length	L_l = 300.0 mm
Outer/inner diameter of the liquid line	8.0 mm/6.0 mm
Primary porous layer (see Table 2 for details)	
Thickness	2.0 mm
Diameter	D_{ei} = 68.0 mm
Copper powder particle size	Five particle species are used (see Table 2)
Secondary porous wick	
Thickness	2.0 mm
Diameter	D_{ei} = 68.0 mm
Copper powder size	Average powder diameter of 149 μm
Third layer of wick	
Thickness	2.0 mm
Diameter	D_{ei} = 68.0 mm
Pore size of the absorbent wool	Average pore size of 20 μm

(maximum voltage of 45 V). The power applied to the evaporator is coming from a power-meter reading with an accuracy of 0.5%.

Staring from the vapor outlet port, thermocouples are marked as T_{Eout}, T_V, T_{Cin}, $T_{C1} \sim T_{C4}$, T_{Cout}, T_{CPin} and T_{CP} (see Fig. 3a). T_{Eout} is a jacket thermocouple to measure the vapor temperature near the vapor outlet port. T_V measured the outer wall temperature of the vapor line. T_{Cin} and T_{Cout} measured the condenser tube temperature at the condenser inlet and outlet, respectively. $T_{C1} \sim T_{C4}$ measured the tube wall temperatures on the four tube bending sections. T_{CPin} measured the wall temperature of liquid line near the liquid inlet

port. T_{CP} measured the liquid temperature inside the compensation chamber. Cross sections B-B and C-C show the temperature measurements of T_{Eout} and T_{CP} (see Fig. 3c and d).

Fig. 3b shows locations of nine thermocouples on the evaporator bottom wall. A miniature hole was drilled on the film heater center. Thus a thermocouple wire (T_C) penetrates the film heater to directly measure the evaporator center wall temperature. T_C has the maximum temperature around the loop. Other temperatures ($T_1 \sim T_8$) are marked in Fig. 3b. All the thermocouples are directly welded on the wall surface, except T_{Eout} and T_{CP}. Thus there are no thermal contact resistance between thermocouples and wall.

2.2. The evaporator

Microchannels near the evaporator wall were replaced by modulated porous wick. Benefits of the modulated porous wick with periodically sintered porous stacks and vapor channels are to: (1) omit the thermal conduction resistance of microchannel fins; (2) separate flow paths of vapor and liquid, with vapor venting in vapor channels and liquid suction within porous stacks. These benefits will be verified in Section 3.

Table 2 shows structures adjacent to the evaporator wall. MWE (microchannel/wick evaporator (run 1 for conventional design) was fabricated for comparison purpose, in which the fin height, width and channel width are 1.5, 3.0 and 1.5 mm, respectively, which are the same as those for MBE (run 4). MME (modulated/ monoporous wick evaporator, run 4) used the average particle diameter of 149 µm. Others are MBE (modulated/biporous wick evaporator) with average particle sizes of 88 µm or less (runs 2, 3, 5, 6, 7 and run 4 with d_p = 88 µm or less).

For MME and MBE, porous stack height (h), width (w) and vapor channel width (p) are important parameters. There are no reference values in the literature. Min et al. [10] used the porous height in the range of 0.7~2.0 mm for 2D and 3D modulated porous coatings to enhance pool boiling heat transfer. Ji et al. [11] used modulated porous with triangular vapor channels for pool boiling heat transfer. The porous stack height was 2.5 mm and the pitch width was in the range of 1.0~2.0 mm. Table 2 summarizes values of h, w and p, which are in the millimeter scale, and copper powder diameters. This paper identifies the best parameters for LHP evaporators.

Fig. 4a shows modulated monoporous wick for d_p = 149 µm. Particles are not merged due to their large size, thus there is only one characteristic pore size. Fig. 4b shows the cross section view for d_p = 149 µm, in which porous stack and vapor channel are marked. Sintering small particles forms cluster. The gap between clusters forms large pore, significantly increasing the surface area for liquid film evaporation and acting as the vapor venting path. Small pores can be seen within clusters, increasing the liquid pumping capability due to enhanced capillary force. Fig. 4c and d shows the images for d_p = 37 and 13 µm. Sintering too fine particles easily forms clusters and pores, but small pores between isolated particles are less.

Fig. 5a shows the photo of primary modulated biporous wick sintered on the evaporator wall, before sintering the secondary monoporous wick. The particle diameter is d_p = 88 µm. Fig. 5b shows the SEM image for the microstructure of the porous stack, in which cluster, large pore and small pore are illustrated. The modulated biporous wick has three characteristic sizes: large pores in the scale of several tens of microns, small pores in the micron scale, and vapor channels in the millimeter scale. Vapor channels collect vapor streams from large pores and vent vapor to the condenser. Because evaporation takes place within the modulated porous wick adjacent to the evaporator wall, the vigorous evaporation shortens the heat transfer route in the height direction. Thus the secondary porous layer is cold and functions as the liquid supplier as well as the hydraulic and thermal barriers (see Fig. 2a for the planar view and Fig. 2b for the heat flow, liquid flow and vapor path in the height direction). For our MBE, the secondary monoporous wick was sintered on the first wick layer with an average particle diameter of 149 µm and a thickness of 2.0 mm. The third porous layer used the absorbent wool with an ultra-low thermal conductivity of 0.05 W/m K.

To determine the wick size which decides the maximum capillary pressure on the evaporating surface of the wick, we use the first condition for LHP operation which is
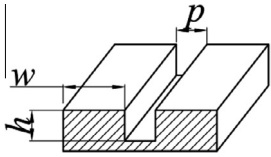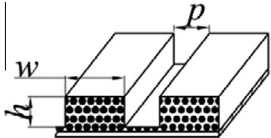
$$\Delta P_c = \frac{2\sigma}{r} \geqslant \Delta P_{tot} \qquad (2)$$

where ΔP_c is the maximum capillary pressure developed on the evaporating surface of the wick, σ is the fluid surface tension, and r is the curvature radius of a meniscus on the evaporating surface of the wick and is essentially half of the mean pore size of the wick. ΔP_{tot} is the pressure drop along the total working fluid path including filtration pressure drop.

On the other hand, the saturation pressure difference corresponding to the saturation temperature difference between the evaporating surface of the wick and compensation chamber is

$$\Delta P_{sat} = P_{sat}(T_v) - P_{sat}(T_{CP}) \geqslant \Delta P_{exit} \qquad (3)$$

Table 2
The structure adjacent to the evaporator wall.

Run	Schematic drawing of the structure adjacent to the evaporator wall	Structure parameter (mm)	Evaporator type and particle size (µm)
1		h = 1.5, p = 1.5, w = 3.0	MWE, the porous wick is above microchannels
2		h = 1.5, p = 1.0, w = 3.0	MBE: 88 (78~92)
3		h = 1.5, p = 1.5, w = 2.0	MBE: 88 (78~92)
4		h = 1.5, p = 1.5, w = 3.0	MBE: 13 (10~14)
			MBE: 37 (25~42)
			MBE: 88 (78~92)
			MME: 149 (75~154)
5		h = 1.5, p = 1.5, w = 4.0	MBE: 88 (78~92)
6		h = 1.5, p = 2.0, w = 3.0	MBE: (78~92)
7		h = 2.0, p = 2.0, w = 3.0	MBE: 88 (78~92)

Note: MWE refers to the microchannel wick evaporator, MBE refers to modulated biporous wick evaporator, and MME refers to modulated monoporous wick evaporator.
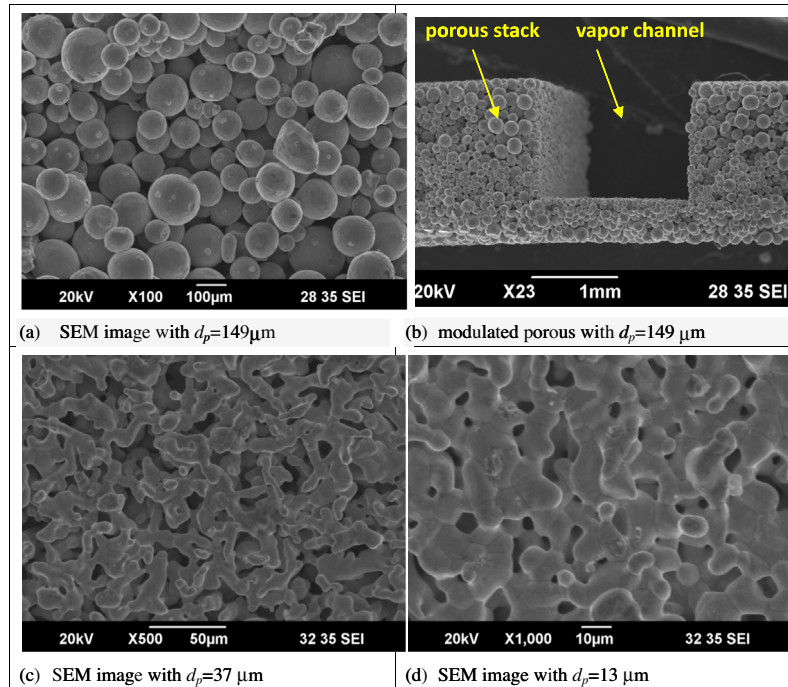
Fig. 4. SEM images for particle sintering with different particle sizes.
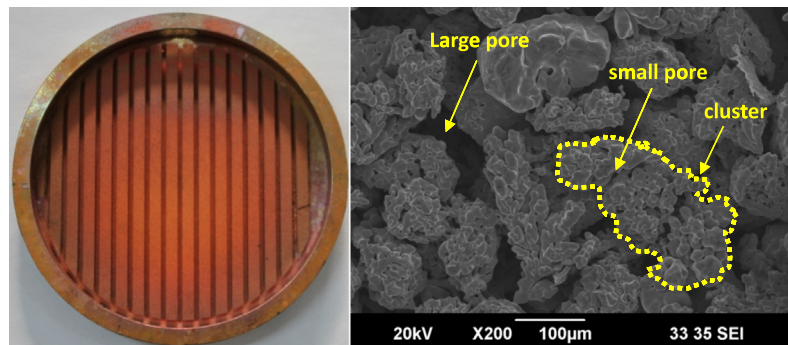

Fig. 5. The photo of modulated porous wick sintered on the evaporator wall (a) and the SEM image within the porous stack (b).

where T_V is the vapor temperature within the porous media of the evaporator and T_{CP} is the temperature in the compensation chamber. ΔP_{exit} is the pressure drop along the external flow path of the working fluid which is the same as the total pressure drop without the filtration pressure drop.

Eq. (2) indicates that a small pore size creates a large capillary pressure for the fluid circulation of the LHP. But the filtration pressure drop is also increased with decreases in the pore size of the wick. Thus, suitable pore size of the wick should be searched for the LHP operation.

2.3. The experiment procedure

The evaporator and compensation chamber were carefully machined. They were consecutively rinsed by methanol and clean water and then they were baked in an oven to keep the components dry. A thin uniform layer of copper powders (about 0.5 mm) was sintered on the internal evaporator wall. A graphite mould was machined to have parallel microchannels, which were filled with copper particles tightly. The evaporator piece and the graphite mould filled with powders were bonded together and

they were put in the oven. The oven was vacuumed and then charged with nitrogen gas to prevent powder oxidization. The four-step-sintering procedure was initiated. The oven temperature was controlled to be 950 °C stably. The sintering process lasted about 4 h. After the sintering was over, the graphite mould was removed to expose the primary modulated porous stacks. The porous porosity was estimated to be 0.32, which is similar to our previous pool boiling experiment [11].

The sodium chloride (NaCl) particles filled the grooves of the first porous wick layer. The copper powders were put on the primary porous wick layer. Then, the evaporator piece was pressed by a ceramic plate, and the sintering process as described above was initiated for the secondary porous wick layer. In summary, the NaCl salt particles were involved in the sintering process of the porous wick.

The evaporator piece with sintered structure, the absorbent wool and the evaporator top piece were packaged to form the evaporator. The evaporator, compensation chamber, condenser (commercial product), vapor line and liquid line were welded together to form the LHP. Attention was paid on the LHP leakage. The LHP was charged with air at a pressure of about 0.3 MPa. If

there were no any bubbles coming out when the LHP was immersed in water for one hour, the LHP was available for experiment.

Water has large surface tension force and latent heat of evaporation. It was used as the working fluid. The deionized water was degassed before charging. The internal LHP volume was about 77.9 ml, summing each component volume, but it is slightly different for different LHPs. The water charged into the LHP was carefully controlled by an electric balance with an accuracy of 0.2 g. The liquid charge ratio (ϕ) is defined as the liquid occupied volume divided by the total LHP internal volume.

This study covers the following data ranges: heat loads = 10~200 W (corresponding to heat flux in the range of 2~40 W/cm^2), liquid charge ratios = 38.5%, 51.3%, 64.1%, 76.9%, tilt angles θ = −90°, −60°, −30°, 0°, 90°. The zero tilt angle refers to the same position of the evaporator and condenser. The positive and negative tilt angles correspond to the evaporator below the condenser and the evaporator above the condenser, respectively. Section 2.2 describes the pressure balance around the LHP. The capillary force is the total driving force to circulate the fluid around the LHP, including the filtration pressure drop. The saturation pressure difference between the evaporator and compensation chamber is the driving force to circulate the fluid around the LHP pipelines, not including the filtration pressure drop.

2.4. Data reduction and uncertainty analysis

The evaporator outer wall was wrapped by the thermal insulation material. The heat flux is defined as the heat load divided by the heating area: $q = Q/A$, where $A = 5$ cm^2. Three thermal resistances are used here. The LHP thermal resistance is

$$R_{LHP} = \frac{[T_C - 0.5(T_{Cin} + T_{Cout})]}{Q} \qquad (4)$$

The numerator of Eq. (4) reflects the temperature difference between the evaporator wall and the condenser wall. The condenser wall temperature is averaged by the wall temperature at the inlet and outlet part. R_{LHP} reflects the combined performance of evaporator and condenser. Chen et al. [12] and Singh et al. [13] used the same definition as Eq. (4) to quantify the LHP thermal resistance.

The total thermal resistance is defined as the temperature difference between the evaporator wall and the environment air divided by the heat load:

$$R_{total} = \frac{T_C - T_{air}}{Q} \qquad (5)$$

The evaporator thermal resistance reflects the evaporator performance only, which is

$$R_{eva} = \frac{T_C - T_{Eout}}{Q} \qquad (6)$$

The evaporator heat transfer coefficient is

$$\alpha = \frac{Q}{A(T_C - T_{Eout})} \qquad (7)$$

Eq. (7) is a basic definition of the evaporator heat transfer coefficient. Physically T_{Eout} should be the saturation temperature of the working fluid within the evaporator porous wick, which is difficult to be measured by the temperature sensor. Instead, we used the vapor venting temperature at the evaporator outlet, T_{Eout}. This causes small deviation from the "true" evaporator heat transfer
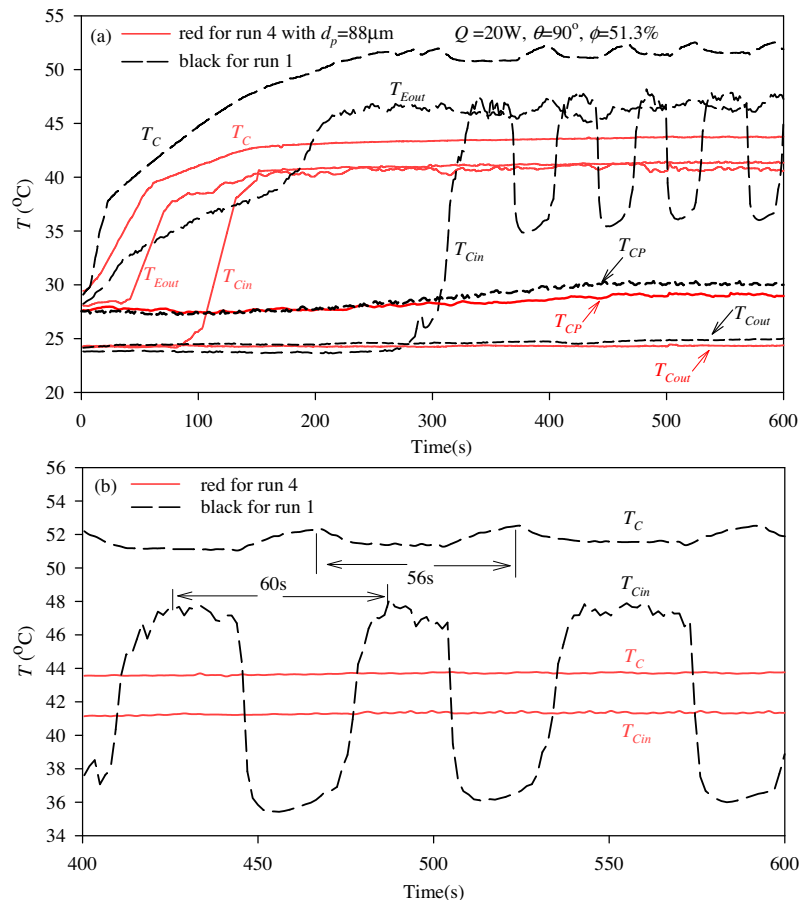

Fig. 6. The start-up for the MWE LHP and MBE LHP.

coefficient because T_{Eout} is very close to the saturation temperature within the porous structure. Refs. [7,14,15] used the same treatment as Eq. (7) to quantify the evaporator heat transfer coefficient.

Uncertainties of the three thermal resistances and heat transfer coefficient can be obtained by performing the standard error analysis. Temperature, heat load, tilt angle, liquid charge ratio, thermal resistance and heat transfer coefficient had the uncertainties of 0.3 °C, 0.5%, 1°, 1.6%, 4.3% and 5.9%, consecutively.

3. Results and discussion

3.1. Start-up process

Fig. 6 shows the start-up for MWE LHP (run 1 in Table 2) and MBE LHP (run 4 with $d_p = 88$ μm in Table 2). Heat load applied to the evaporator at $t = 0$ s. T_{CP} (liquid temperature in the compensation chamber) was about 28 °C, indicating the small heat leakage due to the measures taken reported above. After applying the heat load, the sharp rises of T_C (center wall temperature of evaporator), T_{Eout} (vapor venting temperature) and T_{Cin} (vapor line wall temperature near the condenser inlet) took place at different time. T_C has the quickest response because it is near the heater, and T_{Cin} has the latest response because it is far away from the heater. The LHP start-up time is defined as the time from the applied heat load to the sharp rise of T_{Cin}. The start-up characteristic is obviously different for MWE and MBE LHPs. The start-up time was about 300 s for MWE LHP, but MBE LHP shortened the start-up time to about 110 s. Different from MWE, MBE does not contain microchannel fins, thus it directly receives heat from the heater to initiate the phase change heat transfer within porous stacks. Besides, MBE perfectly stabilize temperature signals after the start-up process is over. Fig. 6b shows the oscillating amplitude of 12 °C and oscillating of about 1 min for MWE (run 1). But all the temperature signals are very stable for MBE (see red curves, run 4). In summary, the modulated porous significantly shortens the LHP start-up time and stabilizes the LHP temperatures during the steady operation. The start-up process at other heat loads and conditions are similar to those shown in Fig. 6.

3.2. The steady thermal performances

3.2.1. Temperature distributions

The following discusses the LHP steady thermal performance. Fig. 7 shows the temperature distributions along the LHP loop for the anti-gravity operation ($\theta = -90°$ in Fig. 7a) and favorable elevation operation ($\theta = 90°$ in Fig. 7b). The z coordinate refers to the extended (stretched) tube length. The modulated porous significantly improves the LHP performance and evens the temperature distributions. For both LHPs, T_C attains maximum value around the loop. MBE significantly reduces the evaporator wall temperatures. For instance, MBE had T_C of only 47 °C at $Q = 80$ W and $\theta = -90°$, but MWE had T_C up to 82 °C at the same condition. Fig. 7 identified the more uniform temperature distribution by MBE. Attention was paid on T_{CP} (liquid temperature in the compensation chamber). The increase of T_{CP} above the room temperature is not obvious at $Q = 20$ W and two tilt angles of 90° and -90° for both LHPs. The situation is changed at high heat loads. The MBE LHP still keeps smaller T_{CP} of 33 °C at $Q = 80$ W, $\theta = -90°$, and 31 °C at $Q = 140$ W, $\theta = 90°$, respectively. Heat leakage was significantly decreased by the MBE LHP at high heat loads. However, the MWE LHP sharply increased T_{CP} to 50 °C and 62 °C (see Fig. 7a and b), indicating larger heat leakage.

As shown by Eq. (3), the decrease of the compensation chamber temperature, T_{CP}, helps to maintain a low saturation temperature within the evaporator porous wick. Thus, it is necessary to keep
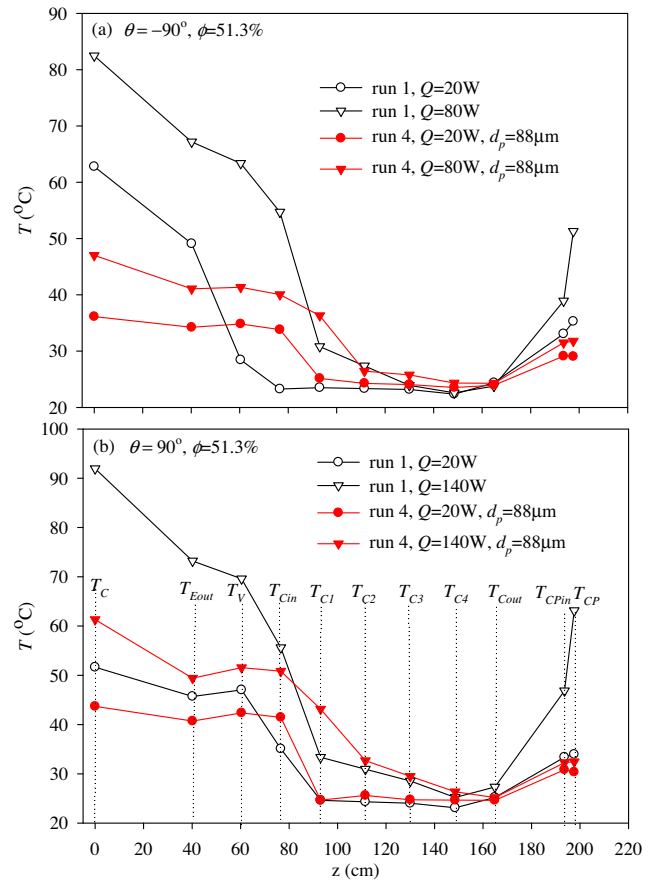

Fig. 7. The temperature distribution around the LHP loop for MWE and MBE LHPs.

the cold operation of the compensation chamber. For instance, Becker et al. [22] applied an external heat exchanger to reduce the compensation chamber temperature. The most important concern is to use the better porous wick structure for the heat transfer enhancement, as reported in this study.

Fig. 8 shows the temperature distribution on the evaporator wall. T_C (evaporator center wall temperature) was the maximum among $T_1 \sim T_4$ and $T_5 \sim T_8$ (see Fig. 3b for locations). Temperatures are more uniform with decreases in heat loads. The modulated porous wick significantly decreases wall temperatures. For instance, MBE had T_C of only 58 °C at $Q = 160$ W and $\theta = -90°$, but MWE had T_C up to 74 °C at smaller heat load of $Q = 40$ W (see Fig. 8a).

3.2.2. The evaporator wall temperatures

The anti-gravity operation ($\theta = -90°$) is a difficult task, due to the fact that the capillary pressure created within the evaporator porous should balance a set of pressure drops. The hydrostatic head of the liquid phase is a major pressure resistance to be overcome. Fig. 9 shows T_C for $\theta = -90°$. Both liquid charge ratios and geometric structure parameters strongly influence T_C. The less liquid charged LHP yields narrow operation range of head loads: heat load less than 80 W (see Fig. 9a). The less liquid charged LHP causes the earlier appearance of dry-out, under which small pores are even occupied by vapor to block the fluid circulation. Alternatively, the over liquid charging at $\phi = 64.1\%$ prevents dry-out at higher heat loads, extending the heat load range to 200 W (see Fig. 9c). The best liquid charge ratio appears at $\phi = 51.3\%$, at which the heat load range is up to 200 W with T_C of only 63 °C, if the porous stacks are properly designed (run 4 in Fig. 9b).
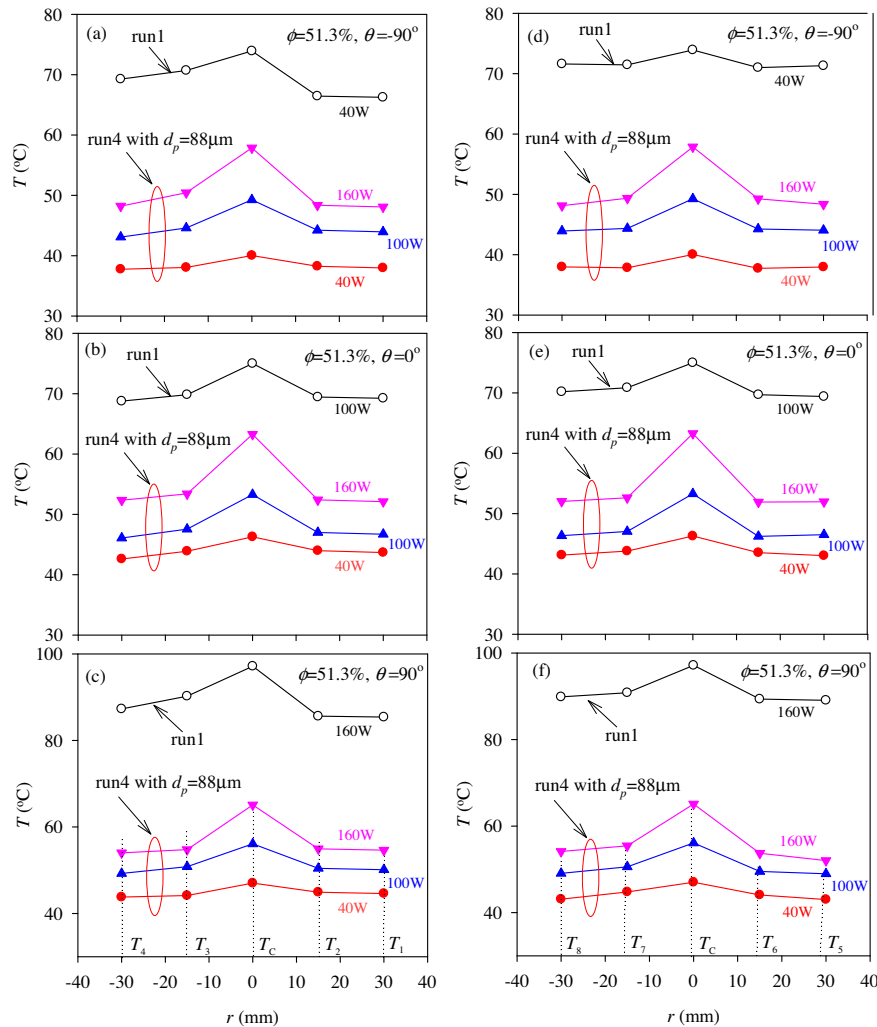
Fig. 8. The temperature distribution on the evaporator wall for MWE and MBE LHPs (*r* is the radial coordinate from the wall center).

Structures near the evaporator wall significantly affect T_C. MWE (microchannel/wick evaporator, run 1) possess higher temperatures than MBE (modulated/biporous wick evaporator, runs 2∼7). The porous stack height (*h*), stack width (*w*) and vapor channel width (*p*) should be synergized to have best LHP performance. The best modulated porous are with *h* = 1.5 mm, *p* = 1.5 mm and *w* = 3.0 mm for run 4. Smaller vapor channel width such as run 2 (*p* = 1.0 mm) or smaller porous stack width (*w* = 2.0 mm) such as run 3 gave poorer LHP thermal performance, compared with run 4. Too large porous stack width (*p* = 4.0 mm for run 5), larger vapor channel width (*p* = 2.0 mm for run 6), and thicker porous stack height (*h* = 2.0 mm for run 7) also deteriorate LHP performance. Wider porous stack width increases the surface area for liquid film evaporation, but hinders the vapor release out of the porous stack. Thus there is an optimal porous stack width. Too narrow vapor channels increase the vapor venting resistance but too wide vapor channels decrease the cross section area of porous stack. Thus there is also an optimal vapor channel width. Too thick porous stack height increases the liquid flow path from the secondary porous layer to the evaporator bottom.

In summary, MWE LHP has poorer thermal performance than modulated porous wick evaporator LHP. The MBE LHP demonstrates the superior anti-gravity operation performance. This is also true for the favorable operation ($\theta > 0°$). The best porous parameters are for run 4 with *h* = 1.5 mm, *p* = 1.5 mm and *w* = 3.0 mm. Because runs 2, 3 and 7 had poorest LHP performance, they are not further analyzed in following sections.

3.2.3. The LHP thermal resistances and evaporator heat transfer coefficients

Fig. 10 shows LHP thermal resistances versus heat loads at three tilt angles of $\theta = -90°$, 0° and 90°. The liquid charge ratio and particle size are optimized to be 51.3% and 88 µm, respectively. Thermal resistances are decreased with increases in heat loads. When the thermal resistance begins to rise, the operation becomes worse and that point is identified as the maximum heat load at which a LHP can sustain. The best MBE LHP (run 4) reach the low evaporator wall temperature of 63 °C and thermal resistance of 0.12 K/W at *Q* = 200 W for the anti-gravity operation. This corresponds to the heat flux up to 40 W/cm². Among runs 1, 4, 5 and 6, MWE LHP (run 1) and MBE LHP (run 4) yield the largest and lowest thermal resistances, respectively. The effect of porous stack and vapor channel parameters on R_{LHP} is decreased when the tilt angles are increased to 0° (horizontal position) and 90° with evaporator below condenser (see the three color curves in Fig. 10b and c). Fig. 10 shows that MWE (microchannel/wick evaporator, run 1) LHP not only has largest R_{LHP}, but also has narrow heat load range, especially for the anti-gravity operation. MBE LHP markedly
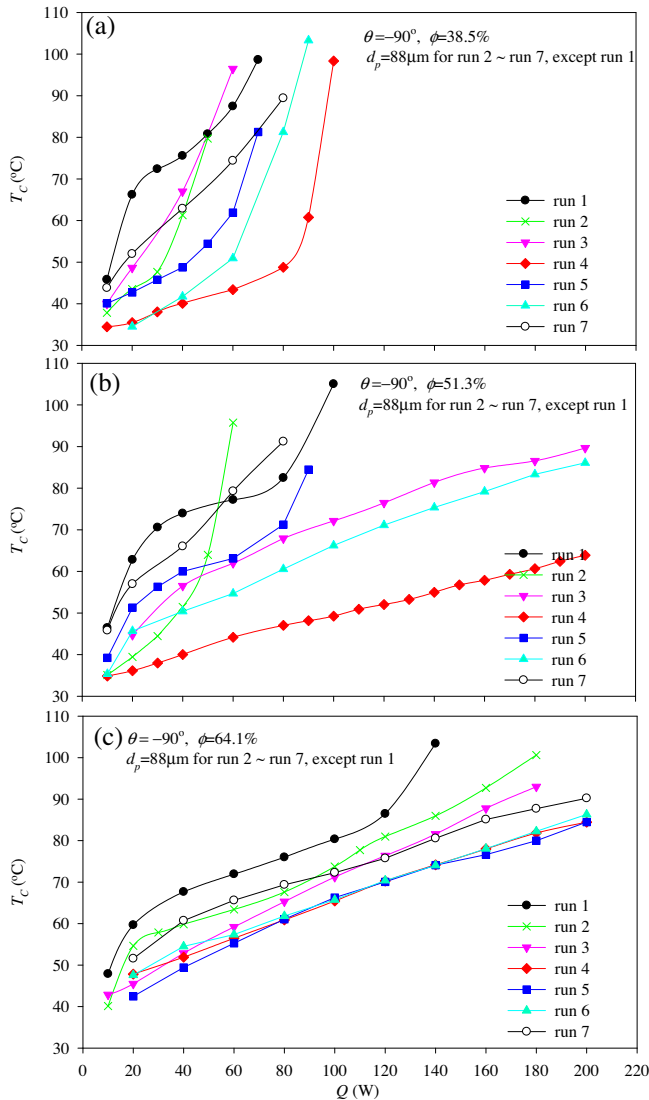
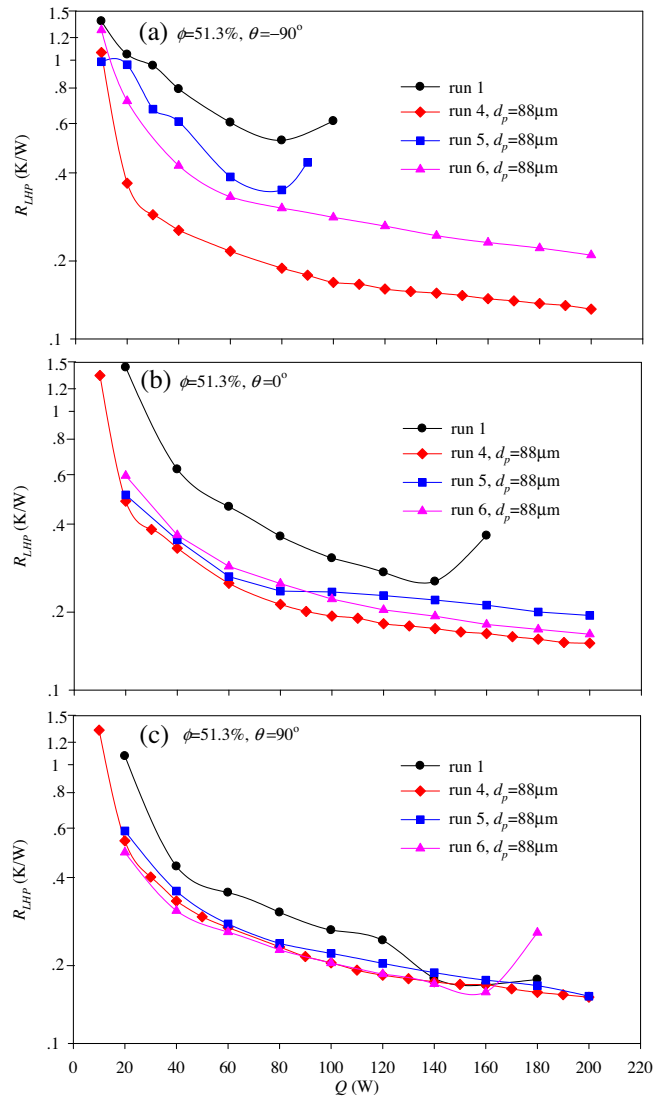Fig. 9. T_C versus heat loads for various LHPs ($\theta = -90°$).

Fig. 10. R_{LHP} versus heat loads at three tilt angles.

decreases R_{LHP} and extends the heat load range, behaving superior performance than MWE LHP.

Fig. 11 shows evaporator heat transfer coefficients versus heat loads for three inclination angles of $\theta = -90°$, $0°$ and $90°$. The heat transfer coefficients for MBE (color curves) are about two times of those for MWE (black curves). For instance, the heat transfer coefficients are about 26~28 kW/m² K for MBE and less than 16 kW/m² K for MWE at $\theta = -90°$ (see Fig. 11a). The other two tilt angles show similar behavior, demonstrating significantly improved heat transfer with modulated porous wick over microchannels. The MBE heat transfer coefficients are larger at $\theta = -90°$ and they are slightly decreased with increases in tilt angles. The surface area for liquid film evaporation is increased with evaporator above condenser ($\theta = -90°$). The evaporator has larger vapor content due to the gravity force induced liquid settlement, yielding large pores between clusters occupied by vapor and liquids only within small pores between particles.

The best liquid charge ratio of $\phi = 51.3\%$ yields larger heat transfer coefficients than less or over liquid charge ratios, for both evaporators. For the less liquid charge ratio of $\phi = 38.5\%$, the MBE heat transfer coefficients are sharply decreased at $Q = 80$ W and $\theta = -90°$ (see Fig. 11a). This is because liquid is not enough and dry-out easily happens within the porous stacks.

Fig. 11 identifies the important heat transfer mechanisms between MWE and MBE. MWE behaves the increased heat transfer coefficients versus heat loads (or heat fluxes), except the decreased heat transfer coefficients near the maximum limit of heat load. This behavior is totally changed by MBE. It is found that the heat transfer coefficients are sharply increased with increases in heat loads at small heat loads. A transition point of heat load is roughly identified beyond which the heat transfer coefficients do not change versus heat loads. This indicates the bubble nucleation heat transfer mechanism at small heat loads (or heat fluxes) and the perfect liquid film evaporation heat transfer mechanism beyond the transition point. For instance, the MBE heat transfer coefficients behave the rise trend with $Q < 60$ W, corresponding to the bubble nucleation heat transfer (region I in Fig. 11a). But heat transfer coefficients are about 26~28 kW/m² K for $Q > 60$ W, corresponding to the film evaporation heat transfer mechanism (region II in Fig. 11a). The transition heat loads are shifted to about $Q = 80$ W at $\theta = 0°$ and $90°$ (see Fig. 11b and c).

3.3. Effect of various parameters

The best MBE porous stacks (run 4) are with $h = 1.5$ mm, $p = 1.5$ mm and $w = 3.0$ mm. This section explains the effect of

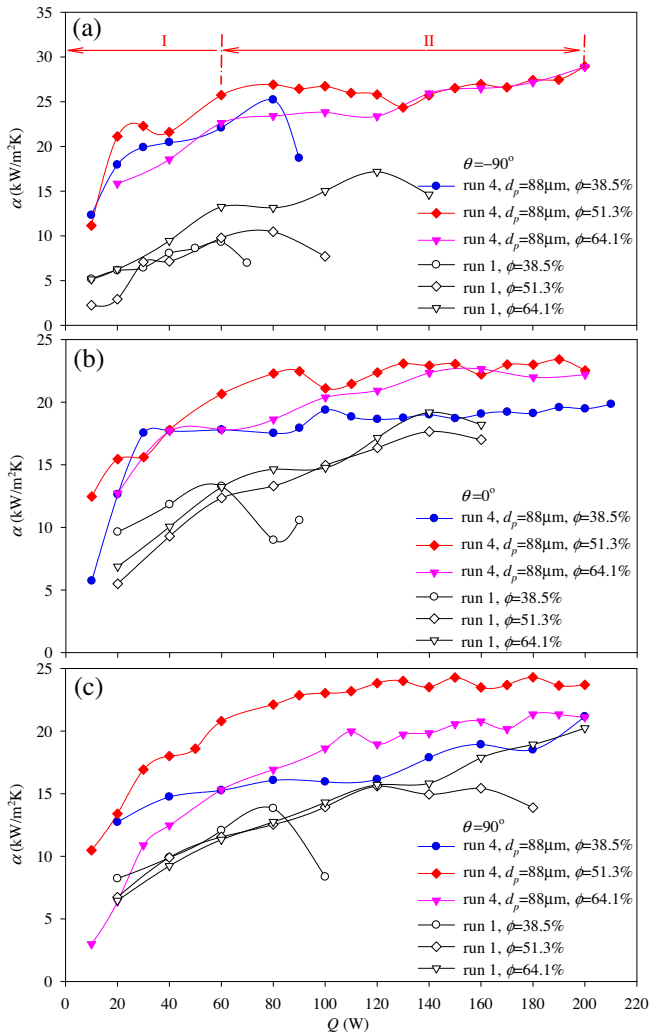**Fig. 11.** Evaporator heat transfer coefficients versus heat loads at various tilt angles and liquid charge ratios.

Fig. 12. Effect of liquid charge ratios on R_{LHP}.

various parameters on the LHP performance focusing on run 4. Fig. 12 illustrates the effect of liquid charge ratios. The best liquid charge ratio is ϕ = 51.3%, at which the LHP thermal resistances decrease with increases in heat loads and the minimum thermal resistance reached 0.12 K/W at θ = −90° (see Fig. 12a). Less or over liquid charge ratios deteriorate LHP performance. Attention was paid to the anti-gravity operation (θ = −90°). The over liquid charge ratio of ϕ = 76.9% significantly increases LHP thermal resistances and shortens the heat load range. One reason is the increased flow resistance around the LHP loop due to the most LHP internal volume occupied by the "heavy" liquid. Besides, heat transfer within the evaporator structure is majorly contributed by thermal conduction while the bubble nucleation or film evaporation heat transfer is difficult to be initiated when the LHP is significantly over charged. Too less liquid charge ratio of ϕ = 38.5% maintains good film evaporation heat transfer thus R_{LHP} is small for the anti-gravity operation. But liquid dry-out takes place earlier at Q = 80 W (see Fig. 12a).

Fig. 13 shows the effect of tilt angles on R_{LHP} and R_{total}. The capillary force within the evaporator porous structure is the driving force to circulate the flow rate around the LHP. Under the anti-gravity operation, the capillary force should balance the hydrostatic head of the liquid phase between the compensation chamber and the condenser. Thus, the flow rate for the anti-gravity opera-
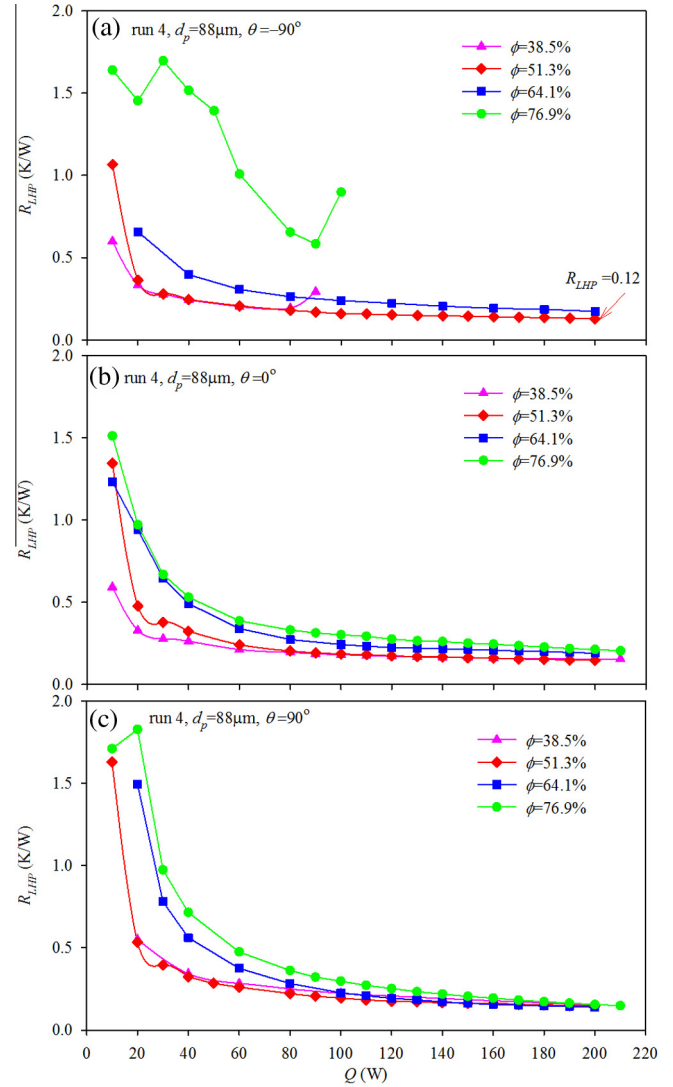
tion should be smaller than that for the favorable level operation. At the same heating power (or heat flux), the anti-gravity operation yields the largest vapor content in the evaporator to provide largest surface area for film evaporation heat transfer. Thus R_{LHP} is the smallest. On the other hand, the favorable level operation (evaporator below condenser) yields the smallest vapor content within the porous wick of the evaporator due to the large circulated flow rate, under which the surface area for film evaporation heat transfer is small. This explains why the favorable level operation has poorer thermal performance than the anti-gravity operation, even though the favorable level operation possesses larger flow rate. This analysis is valid during the LHP start-up and steady operation. Fig. 13 illustrates the improved thermal performance with decreases in tilt angles from 90° to −90° (steady operation data). The dominant mechanism is the enhanced film evaporation heat transfer by the increased vapor content with decreases in tilt angles. Fig. 13 shows that R_{total} is slightly larger than R_{LHP}. This is because R_{total} takes the room air temperature as the reference temperature.

Particle size influences the micro structure of porous stacks. Large particles such as d_p = 149 μm form monoporous stack (see Fig. 4a). There are only two characteristic sizes. Liquid is sucked through micro pores between particles, and vapor is vented in vapor channels. Evaporation takes place at the solid–liquid–vapor
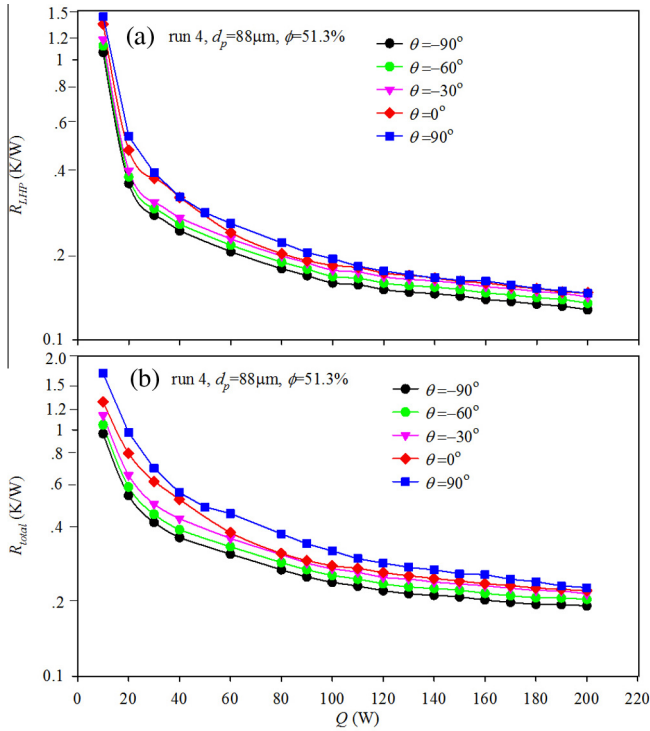
Fig. 13. Effect of tilt angles on R_{LHP} and R_{total}.

interface near the side and bottom porous walls. Because the surface area for film evaporation is limited, the evaporation heat transfer is poorer than biporous stack. The particle size of $d_p = 88$-μm forms biporous stack, increasing the surface area for film evaporation heat transfer. Besides, the liquid suction is enhanced due to small pores between particles. Thus the best particle size was $d_p = 88$ μm (see Fig. 14). Too fine particle (such as $d_p = 13$ μm) sintering yields bonding of particles. Pores exist between particle clusters, but small pores are less, deteriorating the film evaporation heat transfer and liquid suction processes.

3.4. Comparison with other studies

Table 3 summarizes recent studies on LHPs. Evaporators have cylindrical and flat shapes. All belong to MWE (microchannel/wick evaporator). The wick was with copper powder [9,16,17], titanium powder [18], nickel powder [8], metal fiber or mesh screen [19–21]. The condenser either uses the forced convective air cooling [9,17,19,21], or uses the chiller water cooling [16,18,8,20,22]. Some LHP uses water as the working fluid [19], etc. Others use methanol, acetone and ammonia as the working fluids. Some LHPs were tested at horizontal position ($\theta = 0°$ [17,8]), other LHPs were tested for anti-gravity operation ($\theta = -90°$ [19,20], etc.). Detailed study on the effect of tilt angles on the performance is less reported.

Attention was paid on the LHP thermal performance. Usually, heat fluxes dissipated by LHPs are significantly smaller than those for pool boiling heat transfer. This is because the evaporator wick should create enough capillary force to circulate the fluid around the loop. LHPs reached maximum heat fluxes on the order of 10 W/cm² ($q_{max} = 6$ W/cm² by Tang et al. [19], 7.18 W/cm² by Riehl and Dutra [20], 7.96 W/cm² by Tang et al. [9], 7.5 W/cm² by Liu et al. [21] and 6.25 W/cm² by Becker et al. [22]). Other studies reported heat fluxes larger than 10 W/cm² such as 15 W/cm² by Wang et al. [16]. It is noted that the maximum heat fluxes were reached with the evaporator wall temperature beyond the 85 °C
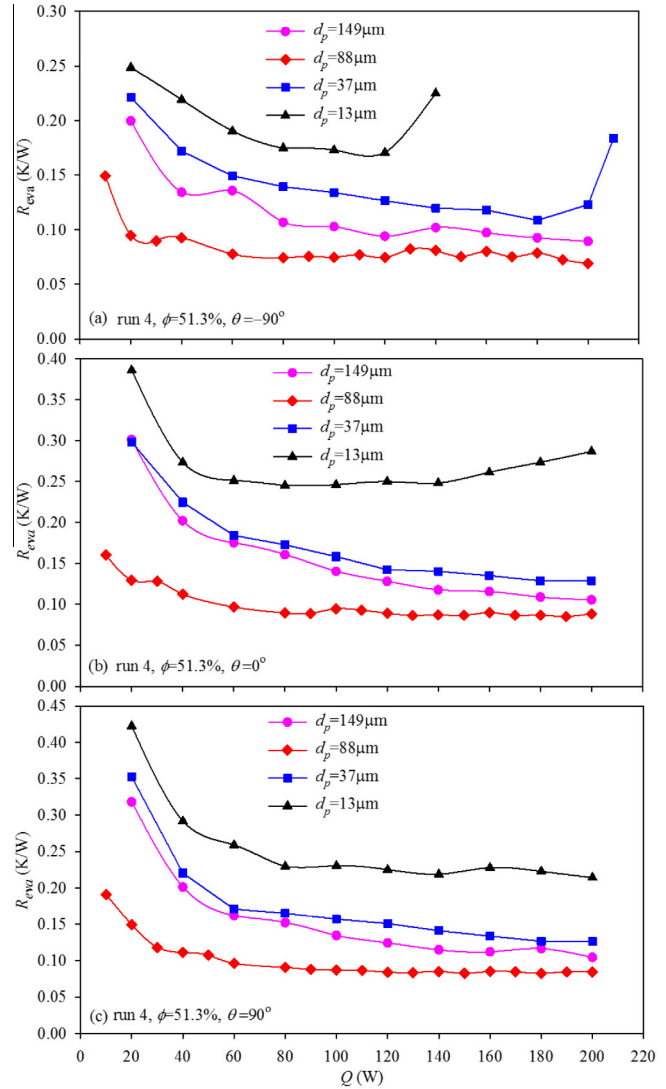

Fig. 14. Effect of particle size on the evaporator thermal resistances.

limit. LHP thermal resistance is another important parameter, which was larger than 0.2 K/W such as 0.38 K/W by Wang et al. [16], 0.4 K/W by Liu et al. [21] and 0.2 K/W by Becker et al. [22].

This study applied modulated porous wick evaporator to replace microchannel/wick evaporator. The evaporator wall temperature reached 63 °C at the heat load of 200 W for the anti-gravity operation. The heat load and heat flux are largest by comparing with those in Table 3. The maximum heat flux of 40 W/cm² at $T_C = 63$ °C is 1.7~6.7 times of those in Table 3. The minimum LHP thermal resistance is 0.12 K/W, which is 26% to 80% of those in Table 3. The following mechanisms account for the significantly improved LHP performance:

(1) *Multiscale porous size*: MBE links three characteristic sizes, with small pores (~μm scale) creating great capillary force acting as the driving force for fluid circulation, large pores (~10 μm scale) between clusters increasing surface area for liquid film evaporation, and vapor channels (~mm scale) for vapor venting. MBE separates flow paths of vapor and liquid.

(2) *Small contact thermal resistance*: MBE sinters the primary and secondary porous layers together. There is small thermal contact resistance within the evaporator.

Table 3
Typical LHP studies reported in the literature.

References	Evaporator	Heat sink	Working fluid and tilt angle	Thermal performance
Tang et al. [9]	Cylindrical eva., MWE, wick with copper powder sintering, $d_p < 75\ \mu m$	Convective air cooling with $T_{air} = 25\ °C$	Water, $\theta = -90°$	$q_{max} = 7.96\ W/cm^2$, $T_c = 78\ °C$ at $Q = 100\ W$, $R_{LHP,min} = 0.15\ K/W$
Wang et al. [16]	Flat eva., MWE, wick with copper powder sintering, 50% porosity	Water cooling with $T_{water} = 25\ °C$	Water, $\theta = -90°$, 0° and 90°	$q_{max} = 15\ W/cm^2$, $T_c = 107\ °C$ at $Q = 110\ W$, $R_{LHP,min} = 0.38\ K/W$
Singh et al. [17]	Flat eva. MWE, wick with copper powder sintering, $d_p = 12\sim15\ \mu m$,	Convective air cooling with $T_{air} = 25\ °C$	Water, $\theta = 0°$	$q_{max} = 16\ W/cm^2$, $T_c = 99\ °C$ at $Q = 60\ W$,
Chen et al. [18]	Cylindrical eva., MWE, wick with Ti powder sintering, $d_p = 17.2\ \mu m$	Water cooling with $T_{water} = 5\sim50\ °C$	Ammonia, $\theta = -90°$, 0° and 90°	$q_{max} = 24\ W/cm^2$, $T_c = 75\ °C$ at $Q = 70\ W$, $R_{LHP,min} = 0.2\ K/W$
Liu et al. [8]	Cylindrical eva., MWE, biporous wick with nickel powder sintering, $d_p = 5\ \mu m$	Cooled by mixture of water and ethylene glycol with $T = -10\ °C$	Methanol, $\theta = 0°$	$q_{max} = 16.8\ W/cm^2$, $T_c = 85\ °C$ at $Q = 160\ W$, $R_{LHP,min} = 0.46\ K/W$
Tang et al. [19]	Flat eva., MWE, wick with metal fiber, $d_p = 200$ and $300\ \mu m$	Convective air cooling with $T_{air} = 25\ °C$	Water, ethanol, $\theta = -90°$	$q_{max} = 6\ W/cm^2$, $T_c = 93.2\ °C$ at $Q = 150\ W$, $R_{LHP,min} = 0.315\ K/W$
Riehl and Dutra [20]	Cylindrical eva., MWE, wick with 304L mesh screen	Bath cooling with water and ethylene glycol, $T_{bath} = -5\ °C$	Acetone, $\theta = -90°$	$q_{max} = 7.18\ W/cm^2$, $T_c = 70\ °C$ at $Q = 80\ W$
Liu et al. [21]	Flat eva., MWE, wick with 82 layers 500 grids stainless steel mesh	Convective air cooling with $T_{air} = 20\ °C$	Methanol and acetone, $\theta = 10°$, 50°, and 90°	$q_{max} = 7.5\ W/cm^2$, $T_c = 52\ °C$ at $Q = 60\ W$, $R_{LHP,min} = 0.4\ K/W$
Becker et al. [22]	Flat eva., MWE, wick with $d_p = 8\ \mu m$	Cooled by a cryostat with liquid circulation, $T = 20\ °C$ and $55\ °C$	Water, $\theta = -90\sim90°$	$q_{max} = 6.25\ W/cm^2$, $T_c = 70\sim90\ °C$ at $Q = 100\ W$, $R_{LHP,min} = 0.2\ K/W$

(3) *Shortcut of the heat flow path*: Direct sintering modulated porous wick on the evaporator wall significantly shortens the heat flow path in the evaporator thickness direction.

4. Conclusions

The periodically arranged modulated porous stacks and vapor channels satisfy the requirement of large vapor channels for vapor venting and small channels for liquid suction. This paper firstly applied the modulated porous wick for LHP evaporator. Conclusions are as follows:

- MBE LHP significantly shortens the start-up time and stabilizes all temperatures during the steady operation.
- MBE LHP keeps significantly low evaporator wall temperatures, which can be decreased by $20\sim50\ °C$ compared with MWE LHP at similar conditions.
- MBE LHP achieved the evaporator wall temperature of only $63\ °C$ at the heat load of 200 W for the anti-gravity operation, under which the heat flux attained $40\ W/cm^2$, which is $1.7\sim6.7$ times of those reported in references. The LHP thermal resistance reached 0.12 K/W, which is only 26% to 80% of those in references.
- MBE behaves two heat transfer mechanisms: nucleate boiling heat transfer at small head loads, and film evaporation heat transfer beyond a transition heat load.
- For a properly designed MBE LHP, it had better performance for the anti-gravity operation than that for the favorable level operation. The LHP thermal resistances are slightly increased with increases in tilt angles.
- The best liquid charge ratio appears at 51.3%. The less liquid charge causes the earlier appearance of dry-out. The over liquid charges sustain large heat loads, but increase the evaporator wall temperatures.
- The best geometric parameters are for run 4 with $h = 1.5$ mm, $p = 1.5$ mm and $w = 3.0$ mm. The best particle size is $d_p = 88$ - μm. Large particles form monoporous stacks, decreasing the surface area for film evaporation and liquid suction capability. Too fine particles form clusters, but small pores can be less, influencing the liquid supply towards the phase change area.

References

[1] L.L. Vasiliev, Heat pipes in modern heat exchangers, Appl. Therm. Eng. 25 (2005) 1–19.
[2] E. Meléndez, R. Reyes, The pool boiling heat transfer enhancement from experiments with binary mixtures and porous heating covers, Exp. Therm. Fluid Sci. 30 (2006) 185–192.
[3] Y.F. Maydanik, S.V. Vershinin, M.A. Korukov, J.M. Ochterbeck, Miniature loop heat pipes – a promising means for cooling electronics, IEEE Trans. Compon. Pack. Technol. 28 (2) (2005) 290–295.
[4] P.C. Gian, C. Maurizio, F. Massimo, Experimental tests of a stainless steel loop heat pipe with flat evaporator, Exp. Therm. Fluid Sci. 34 (2010) 866–878.
[5] F.C. Lin, B.H. Liu, C.T. Huang, Y.M. Chen, Evaporative heat transfer model of a loop heat pipe with bidisperse wick structure, Int. J. Heat Mass Transfer 54 (2011) 4621–4629.
[6] T. Semenic, I. Catton, Experimental study of biporous wicks for high heat flux applications, Int. J. Heat Mass Transfer 52 (2009) 5113–5121.
[7] C.C. Yeh, C.N. Chen, Y.M. Chen, Heat transfer analysis of a loop heat pipe with biporous wicks, Int. J. Heat Mass Transfer 52 (2009) 4426–4434.
[8] Z.C. Liu, H. Li, B.B. Chen, J.G. Yang, W. Liu, Operational characteristics of flat type loop heat pipe with biporous wick, Int. J. Therm. Sci. 58 (2012) 180–185.
[9] Y. Tang, R. Zhou, L.S. Lu, Z.C. Xie, Anti-Gravity Loop-shaped heat pipe with graded pore-size wick, Appl. Therm. Eng. 36 (2012) 78–86.
[10] D.H. Min, G.S. Hwang, Y. Usta, O.N. Cora, M. Koc, M. Kaviany, 2-D and 3-D modulated porous coatings for enhanced pool boiling, Int. J. Heat Mass Transfer 52 (2009) 2607–2613.
[11] X.B. Ji, J.L. Xu, Z.W. Zhao, W.L. Yang, Pool boiling heat transfer on uniform and non-uniform porous coating surfaces, Exp. Therm. Fluid Sci. 48 (2013) 198–212.
[12] B.B. Chen, Z.C. Liu, W. Liu, J.G. Yang, H. Li, D.D. Wang, Operational characteristics of two biporous wicks used in loop heat pipe with flat evaporator, Int. J. Heat Mass Transfer 55 (2012) 2204–2207.
[13] R. Singh, A. Akbarzadeh, M. Mochizuki, Operational characteristics of a miniature loop heat pipe with flat evaporator, Int. J. Therm. Sci. 47 (2008) 1504–1515.
[14] Y.F. Maydanik, S.V. Vershinin, M.A. Korukov, J.M. Ochterbeck, Miniature loop heat pipes-a promising means for cooling electronics, IEEE Trans. Compon. Packag. Technol. 28 (2005) 290–296.
[15] J.H. Liou, C.W. Chang, C. Chao, S.C. Wong, Visualization and thermal resistance measurement for the sintered mesh-wick evaporator in operating flat-plate heat pipes, Int. J. Heat Mass Transfer 53 (2010) 1498–1506.
[16] S.F. Wang, J.P. Huo, X.F. Zhang, Z.R. Lin, Experimental study on operating parameters of miniature loop heat pipe with flat evaporator, Appl. Therm. Eng. 40 (2012) 318–325.

[17] R. Singh, A. Akbarzadeh, M. Mochizuki, Operational characteristics of the miniature loop heat pipe with non-condensable Gases, Int. J. Heat Mass Transfer 53 (2010) 3471–3482.

[18] Y.M. Chen, M. Groll, R. Mertz, Y.F. Maydanik, S.V. Vershinin, Steady-state and transient performance of a miniature loop heat pipe, Int. J. Therm. Sci. 45 (2006) 1084–1090.

[19] Y. Tang, J.H. Xiang, Z.P. Wan, W. Zhou, L. Wu, A novel miniaturized loop heat pipe, Appl. Therm. Eng. 30 (2010) 1152–1158.

[20] R.R. Riehl, T. Dutra, Development of an experimental loop heat pipe for application in future space missions, Appl. Therm. Eng. 25 (2005) 101–112.

[21] Z.C. Liu, D.X. Gai, H. Li, W. Liu, J.G. Yang, M.M. Liu, Investigation of impact of different working fluids on the operational characteristics of miniature LHP with flat evaporator, Appl. Therm. Eng. 31 (2011) 3387–3392.

[22] S. Becker, S. Vershinin, V. Sartre, E. Laurien, J. Bonjour, Yu.F. Maydanik, Steady state operation of a copper water LHP with a flat-oval evaporator, Appl. Therm. Eng. 31 (2011) 686–695.